Artificial Spacetimes for Reactive Control of Resource-Limited Robots

William H. Reinhardt[1] and Marc Z. Miskin[1*]

[1]Department of Electrical and Systems Engineering, University of Pennsylvania, Philadelphia, 19104, PA, USA.

*Corresponding author(s). E-mail(s): mmiskin@seas.upenn.edu;
Contributing authors: whr@seas.upenn.edu;

Abstract

Field-based reactive control provides a minimalist, decentralized route to guiding robots that lack onboard computation. Such schemes are well suited to resource-limited machines like microrobots, yet implementation artifacts, limited behaviors, and the frequent lack of formal guarantees blunt adoption. Here, we address these challenges with a new geometric approach called artificial spacetimes. We show that reactive robots navigating control fields obey the same dynamics as light rays in general relativity. This surprising connection allows us to adopt techniques from relativity and optics for constructing and analyzing control fields. When implemented, artificial spacetimes guide robots around structured environments, simultaneously avoiding boundaries and executing tasks like rallying or sorting, even when the field itself is static. We augment these capabilities with formal tools for analyzing what robots will do and provide experimental validation with silicon-based microrobots. Combined, this work provides a new framework for generating composed robot behaviors with minimal overhead.

1 Introduction

Microrobots hold significant promise for a variety of applications including drug-delivery [1, 2], environmental remediation [3, 4], and micro-manufacturing [5]. However, their small size imposes significant limitations for onboard computation, sensing, and actuation, making many traditional control architectures difficult to implement. As a result, new and unique strategies are required to guide robots too small to see by eye.

The majority of existing microrobot control schemes fall into two groups: top-down and reactive. In top-down control, an external system continuously monitors each robot and directly updates forcing fields that guide it toward a desired state. These approaches, often implemented using optical tweezers [6], electromagnetic actuation [7, 8, 9, 10], and/or acoustic fields [11, 12, 13], provide precise and adaptable control, making them well-suited for complex, multi-step tasks or those requiring high accuracy. However, existing implementations struggle with accommodating large numbers of independent microrobots, as many of the forcing fields are hard to spatiotemporally pattern and face trade-offs between resolution and field of view when scaled to large workspaces [14, 15]. Further compounding these challenges is the fact that top-down approaches often require extensive calibration or bespoke pieces of laboratory equipment to implement.

Reactive control strategies provide a complementary approach that could help address these shortcomings, emphasizing parallelism and decentralization. Rather than relying on continuous external feedback, they use on-robot sensory inputs to immediately modulate the robot's actions in response to a global control field. Common examples are stimuli-responsive micromotors that achieve taxis [16], artificial potential fields that coordinate motion through attractive and repulsive forces [17], and micro-robot swarms whose behavior emerges through collective interactions [18, 19, 20, 21]. Because each robot executes actions without waiting for a central controller, these approaches reduce implementation overhead and enable swarms of microrobots to operate in parallel without individualized tracking and intervention. Furthermore, many microrobots are made from field-responsive engines [22, 23, 16], making reactive control a natural framework.

A major challenge for reactive control is building fields that promote sophisticated actions. While a variety of work has demonstrated simple behaviors (e.g., taxis) [16, 24, 25], it remains difficult to realize complex tasks like navigating a structured environment or independently guiding multiple agents to distinct places using a single, static field. Further, many algorithms for reactive control are heuristic, lacking formal guarantees and suffering from implementation artifacts (e.g., local minima) unless further optimized [26, 27, 28]. In cases where control fields do yield desired results, it is challenging to port the solution to a new problem, often requiring fields to be redesigned to match each application.

In this work, we propose a new approach to creating reactive control fields, called artificial spacetimes, which lends itself to addressing some of these issues. Specifically, this geometric framework allows us rationally construct fields that Braitenberg-like robots [29] can use to carry out tasks in structured environments, offers formal methods

for analyzing what a robot will do and when, and enables solutions to be reused across problems.

Our starting point is the observation that the trajectories of certain robots under reactive control in slowly-varying fields are formally equivalent to null geodesics on a Lorentzian manifold [30, 31]. From this point of view, control fields set up local metric tensors while reactive robots follow paths of minimal space-time interval. This connection, while surprising, enables us to leverage specialized coordinate transformations and well-studied metrics from optics and relativity to solve various control problems. For instance, we present metrics that enable robots to rally, confine, or turn in prescribed ways. Further, we are able to embed boundary avoidance within the same control field without sacrificing the desired behavior. In other words, these results can be composed with one another, enabling fields that simultaneously prevent robot collisions with walls and give instructions for navigation, localization, and/or sorting without requiring explicit on-robot computation. In addition to theoretical results, we validate this framework through both simulations and experiments with microrobots. Combined, these results show a promising new way to extract interesting behaviors from small robots that lack the ability to compute.

2 Results

In Figure 1a, we outline the kinematics for a common robot design that maps its local sensory inputs to motor speed (commonly known as a Braitenberg vehicle [29]). The robot has two motors that each move at their own velocity depending on the sensory intensity $I(x)$ (e.g., light intensity). The body of the robot traces a path in two dimensions with curvature κ, proportional to the normalized difference in motor velocities, at a speed V_B equal to the average speed of the two motors. When placed in a spatially varying sensor field, visualized in Figure 1a, the robot turns due to the unequal stimulation of the motors. We note that despite having no onboard computer or memory system, a robot navigating in this way remains under closed-loop control; the robot takes local measurements of its environment and its speed and direction are modulated in response.

With an eye towards microrobots, we consider the case that the sensory field varies slowly in space relative to the size of the robot. In other words, variation in I takes place over a much larger length scale than the robot's size. Under this assumption, I can be approximated locally by a Taylor series, leading to equations (see SI) for the robot's acceleration (equation 1) and speed (equation 2):

$$I\frac{d^2 x_i}{ds^2} = \epsilon_{ij}\frac{dx_j}{ds}\left(\frac{dx_l}{ds}\epsilon_{lm}\partial_m I\right)$$ (1)

$$\frac{ds}{dt} = I(x_i)$$ (2)

where s is the arclength traveled by the robot, x is its coordinate position, and ϵ_{ij} is a 90° counter-clockwise rotation matrix.

Both equations are strongly reminiscent of Lorentzian geodesics. First, equation 1 is structurally consistent with the general form of a geodesic: the right hand side

3

is quadratic in the coordinate velocities while the left hand side is an acceleration. Second, equation 2 can be rewritten as $I^2(x, y)dt^2 - dx^2 - dy^2 = 0$ by squaring both sides. This form shows the robots next positions are constrained to a cone of accessible spatiotemporal locations, a hallmark of Lorentzian geometry. The cone's opening angle varies in space and time, controlled by the sensory field I, and, as visualized in Figure 1b, the robot's trajectory is defined by where these cones meet. Indeed, prior work [32, 33] has shown surprising experimental connections between differential drive macro-scale robots and relativistic physics, suggesting the possibility of a formal relationship.

Together, these observations strongly suggest that the robot's motion could be derived by minimizing an action on an appropriately curved spacetime. By applying calculus of variations to the metric implied by equation 2, we find this the correspondence is exact: the robot's motion is formally identical to the path light takes in a curved spacetime (see SI for derivation).

Connecting the path of a reactive control robot to a Lorentzian geodesic brings significant formal structure. One can use known symmetries in the spacetime to predict how long it will take a robot to traverse a path or predict whether a region of space is asymptotically attracting. Crucially, the numerous symmetries, intuitions, and solved problems from both relativistic mechanics and ray optics can be appropriated for the task of engineering robot behaviors.

As an example, we analyze a proportional control field intended to guide robots to the origin from the point of view of Lorentzian geodesics. Specifically, we take the sensory field $I = \sqrt{x^2 + y^2} = r$ such that each motor's velocity is proportional to its distance from the target location. Heuristically, this scheme aims to both align robots to the target location and slow them down as they approach.

Using our geometric formalism, we determine the range of initial headings and positions that are guaranteed to arrive at the origin and their rate of convergence. Since this metric depends only on the radial distance, the dynamics conserve both energy $E = -r^2 dt/d\lambda$ and angular momentum $L = r^2 d\phi/d\lambda$ where λ is an affine parametrization and ϕ is the angle between the robot's position and the origin. Using these symmetries and the null-affine parametrization $d\lambda = I^2 dt$ [34], equation 2 simplifies to a first order equation for the radial velocity (see SI for details)

$$(\frac{dr}{dt})^2 = r^2(1 - L^2) \tag{3}$$

Since the sign of the right hand side of eqn. 3 cannot pass through zero, robots cannot change whether they are headed towards or away from the origin. Indeed, explicitly computing the angular momentum gives $L = \sin(\alpha_0)$ where α_0 is the initial misalignment between the robot's heading and its radial vector (see SI for details); the phase space is always split between strictly ingoing and outgoing paths.

Focusing on the inward falling trajectories, we directly compute the rate of convergence. Integrating eqn. 3, we find $r(t) = r_0 \exp[-t \cos(\alpha_0)]$. In other words, any robot with an initial misalignment between $+\pi/2$ and $-\pi/2$ converges exponentially fast to the origin, regardless of its initial distance from the target location. Figure 1c and

Figure 1d show simulations of robots compared to the theory, validating the result. No fit parameters are used.

This simple example hints at how Lorentizian geometry can address control problems. Yet, the use of symmetry arguments raises the question of how to handle more realistic geometries. A structured environment like a maze would clearly lack the radial symmetry of an unobstructed position control problem.

This issue can be resolved by leveraging the coordinate invariance of geodesic motion and light-like trajectories [35, 31]. By properly choosing a new set of coordinates, complex boundaries can be mapped into simple ones, extending the reach of rudimentary control fields. One particularly powerful class of transformations are those that locally preserve angles, or conformal transformations. By definition, a conformal transformation from $x \to \tilde{x}(x)$ transforms the spacetime interval as $d\tilde{s}^2 = ds^2 \Omega^2(x)$. Because the overall effect on the interval is multiplication by scalar function, a null geodesic in one coordinate system remains a null geodesic in the transformed space. The value arises from the fact that many known conformal transformations map complicated boundaries (e.g., arbitrary polygons) to trivial ones (e.g., a disk). Of note, conformal mapping of geodesics is used extensively in optics to build devices ranging from lenses to mirrors to cloaks [31, 36, 37, 38] and transformations can often be generated with computationally efficient algorithms (e.g., root-exponential convergence to solutions) [39, 40, 41].

This invariance property presents a two-stage composition procedure for building reactive control fields, illustrated schematically in Figure 2. First, encode all the boundary information via conformal transformation to a simple virtual space. In virtual space, implement the desired behavior with a control metric. The conformal transformation can then be inverted to map the control law back to physical space, resulting in a composite metric that expresses both the desired behavior and stores information about how to avoid obstacles.

As proof of this approach, we simulate robots, governed by equations 1 and 2, navigating non-trivial boundaries under reactive control. We first demonstrate the task of maze traversal by mapping the maze to a rectangular virtual space, imposing the proportional control metric, and inverting the transform to build the control field for physical space (see SI). As seen in Figure 3a, three robots with different initial positions trace out the maze and reach the target location. While virtual space shows essentially the same behavior as trajectories in Figure 1c, guiding robots to the goal, the mapping back to physical space adds the missing information needed for robot to avoid collisions with the walls.

This two-stage approach can be used with other virtual space metrics to complete tasks besides position control. For instance, metrics, originally developed for optics, exist to rally, confine, rotate, or deflect trajectories [42, 43, 44, 45, 46, 47, 48]. The paths in Figure 1a and Figure 1b are characteristic, showing robots patrolling a circular region [49] and focusing them to patrol along a linear path [50, 51], respectively. Applied in virtual space, these same functionalities can be composed with wall avoidance to create more sophisticated behaviors. For instance, Figure 3b shows a metric that turns robots by a fixed amount based on their incident heading in virtual space.

Mapped to real space, robots get sorted upon exiting a junction, each arriving at a unique position despite the fact that they use the same static control field.

As a final test of our framework, we present experimental studies on microscale robots, showing their applicability in the physical world. We fabricate (see SI) silicon-based microrobots (Figure 4a) that use electrokinetic motors in solution to move around their environments [23]. As in the model, each robot has two motors, made up of discrete arrays of silicon photovoltaics, that move at speeds proportional to incident light intensity. We utilize the optical setup in Figure 4a to project spatially varying intensity fields on the bottom surface of petri dish that holds the robot (see SI), enabling us to establish tunable metrics.

We find agreement between the measured robot trajectories and light-like geodesics predicted by our theory. Figure 4b shows several control fields corresponding to oscillatory motion along a linear axis [52, 50, 51], orbiting trajectories [49], and fixed-angle turning [53, 54]. Comparing to simulated trajectories (Figure 4b, bottom), we find agreement. For example, the 90° turning metric [53, 54] rotates our robot's heading $\approx 82°$, with the robot path falling on a simulated geodesic. Further, as seen in the simulation, the behavior is relatively insensitive to the initial heading and provides approximate 90° turns for a 40° window of entry angles, suggesting this strategy could be deployed without precise knowledge of the robot's initial orientation.

Metrics can also be directly joined in space, provided they either extrapolate to a constant value or share a boundary with the same overall intensity field values. To demonstrate, we place two 90° turning lenses next to each other (Fig. 4b). Similar to optics where lenses can added or removed from the beam path to change the overall behavior, the adjacent control gradients yield a composite effect, turning the robot by a full 180°. In addition to being fairly insensitive to the input angle, control metrics can accept a range of input positions while retaining their functionality. For example, in Figure 4b, robots with initial positions spanning approximately 33% of the lens width are rotated and output with a much narrower spread ($\sim 15\%$ of the width).
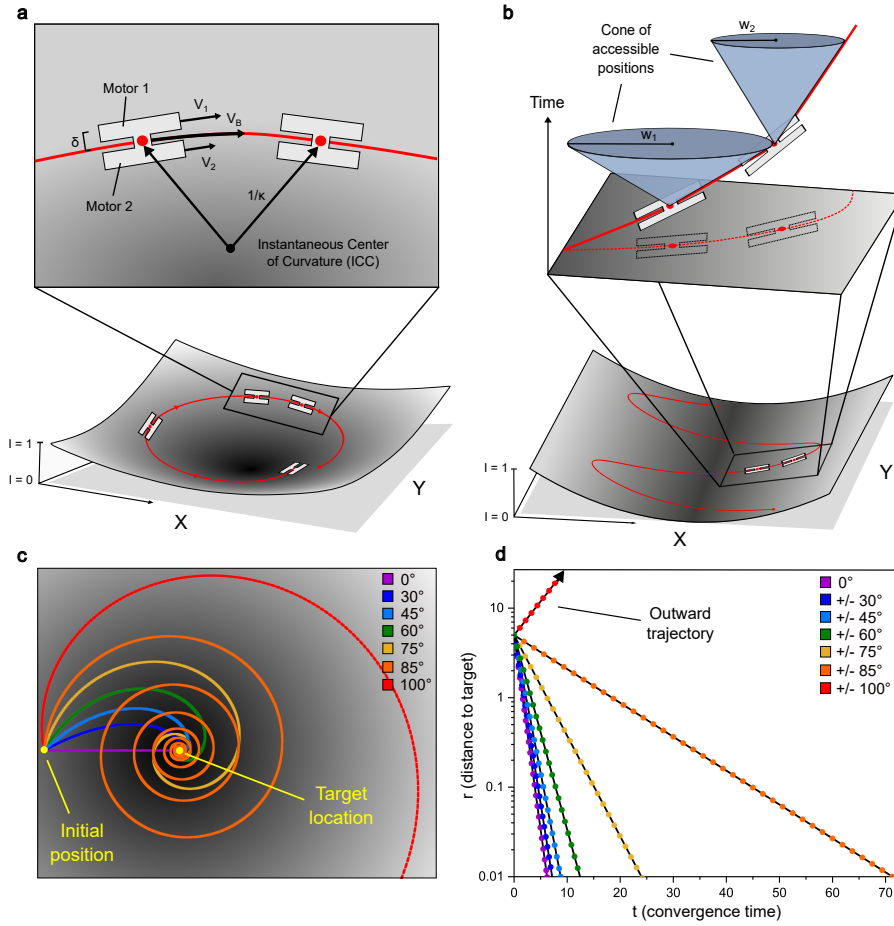
3 Discussion

Artificial spacetimes provide a versatile framework for controlling robots that lack the capacity to compute. Long term, our control strategy could potentially enable microrobots to traverse anatomical structures for drug delivery or cover specific areas in environmental remediation applications without explicit knowledge of the robot's location. Such results could even find use for microrobots with on-board computation [55, 56], reducing memory requirements by offloading the information required for navigation into a sensory field.

While here we have focused on a specific robot class (i.e., Braitenberg vehicles in 2D), there are several promising paths towards generalization. One route could extend the metrics to vary in time. Many applications of autonomous robots require multiple, conditioned, sequential steps. As the manifold here is fundamentally spatiotemporal, it may be possible to encode some of these actions as temporal variations in I without losing geodesic structure. Work along this route might target robot-to-robot collision avoidance or sequential exploration of space by causing individual robots to speed

up or slow down upon arriving at specific spacetime locations. As an added benefit, temporally varying metrics are of interest in related scientific fields, namely optical metamaterials [57, 58] and experimental analog gravity [59]. As dynamic metrics are generally difficult to realize, robots have a unique opportunity to guide scientific explorations by analogy.
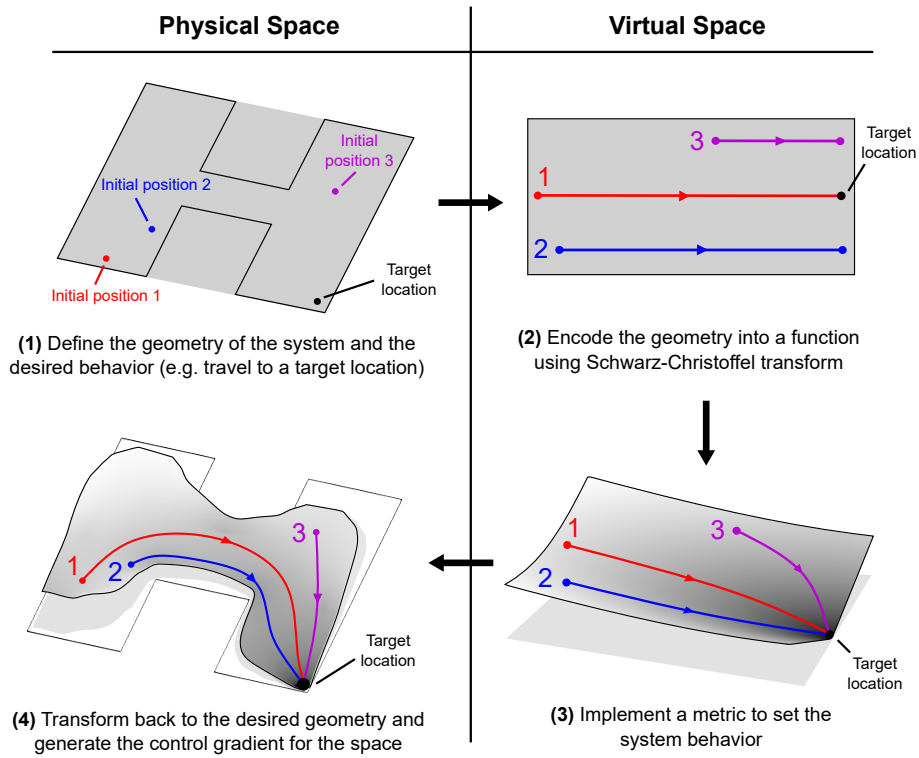
A second generalization could expand the robot hardware. While here we use silicon microrobotics with electrokinetic motors, many microrobot platforms have a mapping between propulsion speed and local measurements like chemical concentration [60], light intensity [22], or temperature [61]. Provided there is a way to create a spatially varying control field, our two-stage composition procedure can be adopted. Alternatively, the governing geometric principles can be generalized to 3D: in the supporting material we specify robot dynamics that extend equations 1 and 2 to produce Lorentzian geodesic motion in three spatial dimensions.

A final generalization could allow robots to establish the control field themselves. While here we project the governing metric onto the system, other works have explored how swarms of reactive robots can realize emergent behaviors by creating their own control fields or interactions [18, 62, 63]. In this case, the geometry couples to what the robots are doing, in effect making the metric a dynamical variable and moving even closer in spirit to general relativity. While the metric dynamics would likely be different, relativistic mathematical and numerical tools might lend themselves to analyzing and controlling the collectively formed geometry, motion, and behaviors.
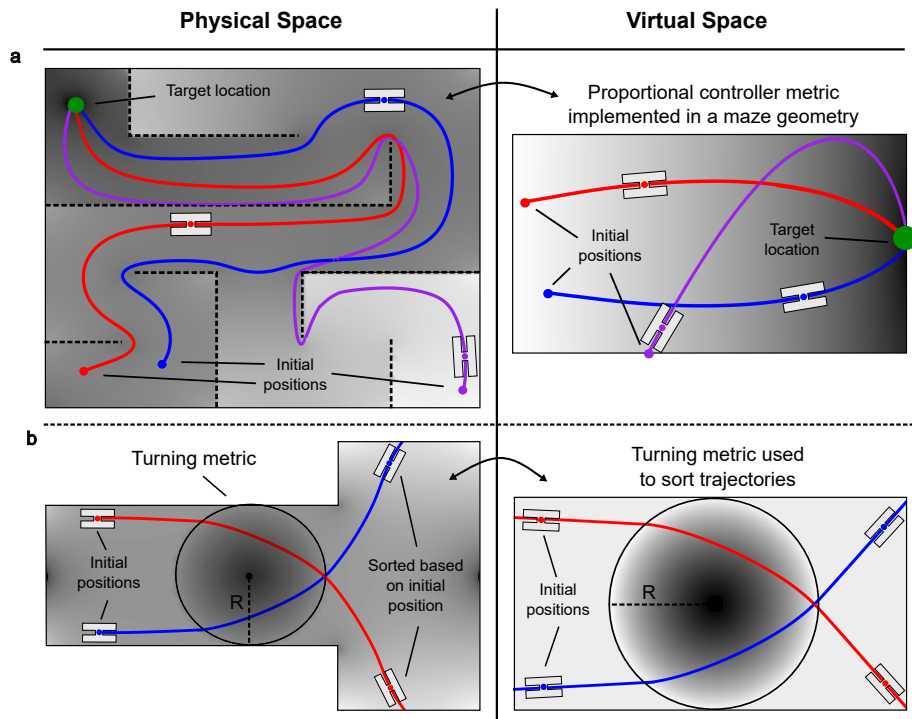
7

Fig. 1 Motion in gradient fields. a) On top, the kinematics of a basic robot with two motors that move at speeds V_1 and V_2. The overall body speed V_B is given by the average of the motor velocities, and the curvature κ is proportional to the normalized difference in motor velocity. The robot's width is given by 2δ. Below, a plot of normalized intensity illustrates the control field in three dimensions. **b)** Plotted with the third dimension of time, robots travel along trajectories connecting cones of accessible positions. The width of the cone w_1 or w_2 depends on the velocity of the robot. **c)** Trajectories with an initial angle in the range $+\pi/2 \rightarrow -\pi/2$ are guaranteed to reach the target location, and trajectories outside of this range escape. **d)** Convergence time for a variety of initial orientations. The black lines are the predicted results for the derived exponential relationship $r(t) = r_0 exp(-t \cos(\alpha_0))$.

Physical Space   **Virtual Space**

(1) Define the geometry of the system and the
desired behavior (e.g. travel to a target location)

(2) Encode the geometry into a function
using Schwarz-Christoffel transform

(4) Transform back to the desired geometry and
generate the control gradient for the space

(3) Implement a metric to set the
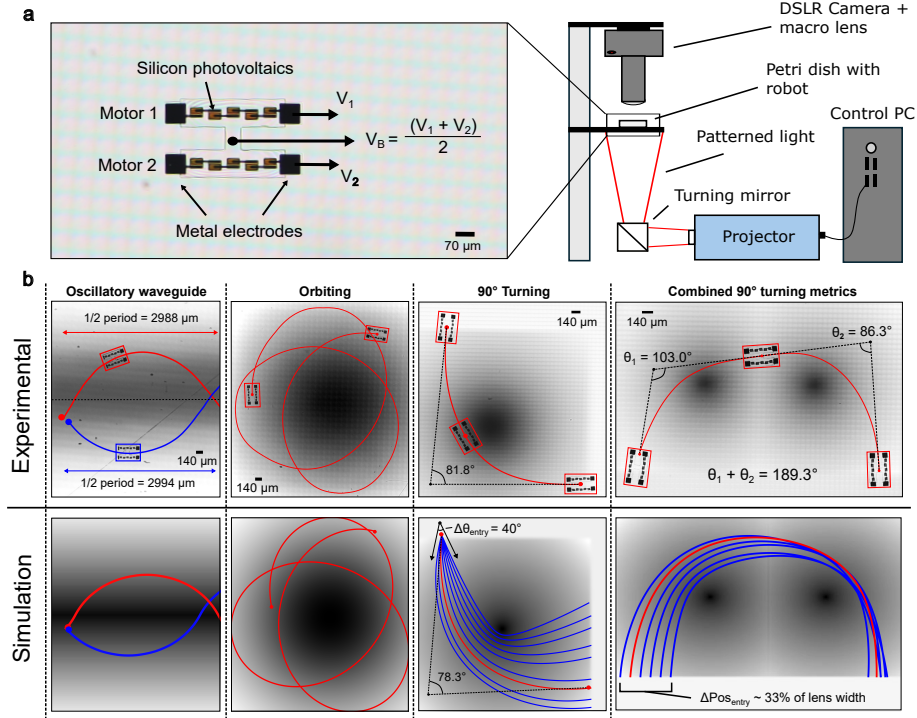system behavior

Fig. 2 Two-stage process to building artificial spacetimes. Coordinate transformations enable
metrics for behaviors to be composed with metrics for boundary avoidance. First, we map a physical
space with a complex boundary to a simple virtual space by a conformal transformation. A control
metrics is then implemented in virtual space to dictate the robot's behavior. For example, here robots
all travel to the target location. When mapped back to physical space, we produce a composite metric
that both encodes the behavior and boundary information in a single scalar field.

9

Physical Space

Virtual Space

a

Target location

Proportional controller metric
implemented in a maze geometry

Initial positions

Target location

Initial positions

b

Turning metric

Turning metric used
to sort trajectories

Initial positions

Sorted based
on initial
position

Initial positions

R

R

Fig. 3 Simulating robot trajectories. a) A maze traversal demonstration with an embedded proportional control metric that directs robots to the same target location. For visualization, the control field magnitude is plotted logarithmically. **b)** A turning metric acts as a sorter that directs robots to different sides of the space based on the initial trajectory. Note both robots use the same static field.

Fig. 4 Experimental demonstrations of the general relativity correspondence. a) A silicon-based microrobot with two electrokinetic motors and differential drive kinematics and an optical setup that creates spatially varying intensity fields. **b)** Experimental demonstrations of various control metrics implemented as intensity fields (top) compared to simulation results (bottom). In the 90° and double 90° turning metric experiments, the simulated traces in red most closely match the initial pose of the experimental demonstration above.

Supplementary information.

Deriving Equations of Motion. We derive the equations of motion for a robot with the kinematics shown in Figure 1a traveling through a spatially varying sensory field. Akin to a differential drive robot, each motor moves at a speed V_1 or V_2. The speed along a path is given as

$$\frac{ds}{dt} = \frac{1}{2}(V_1 + V_2) \tag{4}$$

and the rate of change of the instantaneous center of curvature (ICC) vector is

$$\frac{d\phi}{dt} = \frac{(V_1 - V_2)}{w} \tag{5}$$

defining w as the distance from the center of one motor to the center of the other. We can rewrite equation 5 using the robot's heading vector $\chi = [\cos(\theta), \sin(\theta)]$ where θ is

11

the heading angle with respect to the global coordinate system. By definition of the ICC, $d\theta = -d\phi$, so using the chain rule we get

$$\frac{d\chi_i}{dt} = -[-\sin(\phi), \cos(\phi)]\frac{d\theta}{dt} \tag{6}$$

or equivalently,

$$\frac{d\chi_i}{dt} = \epsilon_{ij}\chi_j\frac{d\phi}{dt} \tag{7}$$

where ϵ_{ij} is a 90° counter-clockwise rotation matrix. Substituting in our definition of $\frac{d\phi}{dt}$, we get a set of motion equations in terms of the motor velocities.

$$\frac{ds}{dt} = \frac{1}{2}(V_1 + V_2) \tag{8}$$

$$\frac{d\chi_i}{dt} = \epsilon_{ij}\chi_j\frac{(V_1 - V_2)}{w} \tag{9}$$

Next, we aim to define these equations in terms of the intensity I. If we assume that the variation in motor speeds comes from a spatial gradient in intensity that is small over the robot's body, we can approximate intensity at a point as

$$I(x, y) \approx I(x_0, y_0) + \partial_i I \Delta x_i + \Delta x_i \partial_{ij} I \Delta x_j \tag{10}$$

To find the average intensity over a motor, we choose $\Delta x_i = \epsilon_{ij}\chi_j(\frac{w}{2}) + \chi_i u$ where u spans the length of the robot body, i.e. $u = [-l/2, l/2]$. We then integrate over u to obtain the average intensity on the motor.

$$I_1 \approx I_0 + \frac{w}{2}\partial_i I \epsilon_{ij}\chi_j + \frac{w^2}{8}\epsilon_{il}\chi_l\partial_{ij}I(\epsilon_{jk}\chi_k) + \frac{l^2}{24}\chi_i\partial_{ij}I\chi_j \tag{11}$$

The intensity over the other motor can be found by setting $w = -w$.

$$I_2 \approx I_0 - \frac{w}{2}\partial_i I \epsilon_{ij}\chi_j + \frac{w^2}{8}\epsilon_{il}\chi_l\partial_{ij}I(\epsilon_{jk}\chi_k) + \frac{l^2}{24}\chi_i\partial_{ij}I\chi_j \tag{12}$$

Assuming light intensity is proportional to motor speed, we can substitute I_1 and I_2 for V_1 and V_2 in equation 8 and equation 9 to get our equations of motion in terms of the intensity,

$$\frac{ds}{dt} = I + \frac{w^2}{8}(\epsilon_{ij}\chi_l)[\partial_{ij}I](\epsilon_{jk}\chi_k) + \frac{l^2}{24}\chi_i[\partial_{ij}I]\chi_j \tag{13}$$

$$\frac{d\chi_i}{dt} = \epsilon_{ij}\chi_j(\chi_l\epsilon_{lm}\partial_m I) \tag{14}$$

In the limit that $w, l \to 0$ and using $\chi_i = \frac{dx_i}{ds}$, the final equations of motion are

$$\frac{ds}{dt} = I(x, y) \tag{15}$$

12

$$I\frac{d^2x_i}{ds^2} = \epsilon_{ij}\frac{dx_j}{ds}(\frac{dx_l}{ds}\epsilon_{lm}\partial_m I(x,y)) \tag{16}$$

Finding Geodesic Equations.   We follow the standard procedure for deriving the geodesic equation by varying the action. Light-like trajectories satisfy the null geodesic condition $g_{\mu\nu}dx^\mu dx^\nu = 0$ where g is the system's metric tensor and $dx^\mu = [dt, dx, dy]$ [30]. Using $I^2(x,y)dt^2 - dx^2 - dy^2 = 0$ from squaring the speed equation, we get a metric

$$g \sim \begin{pmatrix} I^2(x,y) & 0 \\ 0 & -\delta^{ij} \end{pmatrix} \tag{17}$$

We can write the action in terms of the line element ds,

$$S = \int ds^2 \tag{18}$$

To get the geodesic equation, we vary this action with respect to an affine parameterization of the curve, λ,

$$S = \int g_{\mu\nu}\frac{dx^\mu}{d\lambda}\frac{dx^\nu}{d\lambda}d\lambda \tag{19}$$

For the given metric g, we choose a parameterization $d\lambda \propto I^2 dt = Ids$ [34]. Varying the action with respect to x,

$$\frac{d}{d\lambda}[-2\frac{dx}{d\lambda}] = 2I(x,y)\frac{dI}{dx}\frac{dt^2}{d\lambda} \tag{20}$$

Using our parameterization of λ, we can substitute $\frac{dt}{d\lambda} = \frac{1}{I^2}$ and $d\lambda = Ids$ to get

$$\frac{1}{I}\frac{d}{ds}[\frac{1}{I}\frac{dx}{ds}] = -\frac{dI}{dx}\frac{1}{I^3} \tag{21}$$

We apply the chain rule and get

$$\frac{1}{I^2}[\frac{d^2x}{ds^2}] - \frac{1}{I^3}(\frac{dI}{dx}\frac{dx}{ds} + \frac{dI}{dy}\frac{dy}{ds})\frac{dx}{ds} = -\frac{dI}{dx}\frac{1}{I^3} \tag{22}$$

Substituting $1 = (\frac{dx}{ds})^2 + (\frac{dy}{ds})^2$ on the right hand side,

$$\frac{d^2x}{ds^2} - \frac{1}{I}(\frac{dI}{dx}(\frac{dx}{ds})^2 + \frac{dI}{dy}\frac{dy}{ds}\frac{dx}{ds}) = -\frac{dI}{dx}\frac{1}{I}((\frac{dx}{ds})^2 + (\frac{dy}{ds})^2) \tag{23}$$

We can then cancel $-\frac{1}{I}(\frac{dI}{dx}(\frac{dx}{ds})^2)$ from both sides, leaving us with

$$\frac{d^2x}{ds^2} = -\frac{dI}{dx}\frac{1}{I}(\frac{dy}{ds})^2 + \frac{1}{I}\frac{dI}{dy}\frac{dy}{ds}\frac{dx}{ds} \tag{24}$$

Rearranging, we have the light-like geodesic equation for this space,

$$I\frac{d^2x}{ds^2} = -\frac{dy}{ds}\left(-\frac{dx}{ds}\frac{dI}{dy} + \frac{dy}{ds}\frac{dI}{dx}\right) \tag{25}$$

Using the relation $\chi_i = \frac{dx_i}{ds}$, we can rewrite this as

$$I\frac{d^2x}{ds^2} = -\chi_y(-\chi_x\partial_y I + \chi_y\partial_x I) \tag{26}$$

The y component follows a similar derivation, leading to the general equation

$$I\frac{d^2x_i}{ds^2} = \epsilon_{ij}\frac{dx_j}{ds}\left(\frac{dx_l}{ds}\epsilon_{lm}\partial_m I\right) \tag{27}$$

where ϵ is a 90° counter-clockwise rotation matrix. This is identical to the robot's equation of motion, equation 1, derived from differential drive kinematics.

Analysis of the Proportional Metric. Here we provide a detailed derivation of the region and rate of convergence for the proportional control metric, whose spacetime interval is, in polar coordinates:

$$ds^2 = -r^2 dt^2 + dr^2 + r^2 d\phi^2 \tag{28}$$

We can note immediately that the metric does not have any explicit dependence on t or on ϕ. Thus, the dynamics admit two conserved quantities corresponding to the generalized momentum for these coordinates. Explicitly, if we write the action principle as

$$S = \int d\lambda \mathcal{L} = \int d\lambda \frac{1}{2}\left[-r^2\frac{dt}{d\lambda}^2 + \frac{dr}{d\lambda}^2 + r^2\frac{d\phi}{d\lambda}^2\right] \tag{29}$$

Then the momenta $E = \partial_{dt/d\lambda}\mathcal{L} = -r^2 dt/d\lambda$ and $L = \partial_{d\phi/d\lambda}\mathcal{L} = r^2 d\phi/d\lambda$ are constants of motion.

Rather than explicitly solve the geodesics, we can insert these conserved quantities into the null condition for our geodesics. Such an analysis is standard in relativity, and used to determine closest approach in a two-body problem [30].

Specifically, inserting the constants of motion to reduce $-r^2\frac{dt}{d\lambda}^2 + \frac{dr}{d\lambda}^2 + r^2\frac{d\phi}{d\lambda}^2 = 0$ gives us

$$0 = -\frac{E^2}{r^2} + \frac{dr}{d\lambda}^2 + \frac{L^2}{r^2} \tag{30}$$

Finally, we use the known null-affine parametrization for this metric form [34], $d\lambda = I^2 dt = r^2 dt$ to arrive at eqn. 3:

$$\left(\frac{dr}{dt}\right)^2 = r^2(E^2 - L^2) \tag{31}$$

The final steps in our derivation are linking L and E back to robot parameters for comparison. In our explicit affine parametrization, $E = -r^2 dt/(r^2 dt) = -1$ for all initial placements. For the angular part, we find $L = d\phi/dt$. To simplify comparison, we can rewrite this result using the heading vector and initial velocity as

14

$$\frac{d\phi}{dt} = \frac{1}{r^2}[x\frac{dy}{dt} - y\frac{dx}{dt}]] \tag{32}$$

Or noting that $\frac{1}{r}\frac{d\vec{x}}{dt}$ is the normalized heading of the robot $\vec{\chi}$ while $\vec{x}/r = \hat{r}$ we can write

$$L = \hat{r} \times \vec{\chi} = \sin[\alpha_0] \tag{33}$$

where the last line follows as $\hat{r}$ and $\vec{\chi}$ are both unit length.

With the above expressions for L and E we can derive the rate of convergence. Explicitly, eqn. 3, becomes:

$$(\frac{dr}{dt})^2 = r^2(1 - \sin[\alpha_0]^2) = r^2 \cos[\alpha_0]^2 \tag{34}$$

We again note that the right hand side of the expression can only reach zero when the robot halts at the origin. Thus, any in-falling trajectory is always in-falling while any out-falling trajectory is always out-falling. Since the sign of dr/dt is fixed from the initial conditions, we can take the square root of both sides and apply the appropriate sign based on initial orientation. The result is simple first order differential equation for the radial coordinate which is easily solved to give the convergence equation from the main text:

$$r(t) = r_0 \exp[-\cos[\alpha_0]t] \tag{35}$$

As a final comment, we point out that the single-signed nature of convergence is unique to this metric: most others feature a so-called centrifugal barrier in which the conserved angular momentum sets a distance of closest approach. By selecting a proportional metric, we eliminate this problem since the E and L terms in the governing radial equation follow the same functional dependence on R. This eliminates the possibility of a special distance at which dr/dt vanishes, and by extension, precludes turning points.

Generating Intensity Profiles. Recent work in transformation optics has demonstrated the capability to guide and control light by building spatially varying index of refraction profiles. Because our robot's motion is light-like, we can implement these same techniques for robot control. Of note, in this work, there is an inverse relationship between index of refraction and intensity. Light travels slower in a medium with a higher index of refraction, and the robots discussed here travel faster at higher intensity. However, this is simply handled by taking the index of refraction profile n used to guide light and calculating $\frac{1}{n}$ to build an intensity profile.

Many transformation optics components, such as spherically-symmetric lenses and GRIN lenses, have straightforward functions corresponding to their index of refraction profiles [49]. To generate these components as an intensity field, we calculate the profile over a grid of points, take the inverse, and map these values to a grayscale image (0-255). Various components are generated in this way and implemented in Figure 4.

Further, it is well-known in transformation optics how to build an index of refraction profile corresponding to a conformal mapping function w [36, 37, 38]. Simply

15

taking the magnitude of the map's derivative will produce a profile that embeds the coordinate transform, and arbitrary metrics such as proportional controllers can be encoded by multiplying a metric $n_{virtual}$ with this profile, i.e.

$$n_{physical} = n_{virtual}|\frac{dw}{dz}| \tag{36}$$

Again, keeping in mind the inverse relationship between n and I, it is straightforward to build an intensity profile that handles both the geometry of the system and the control law.

Simulating Robot Trajectories. Robot trajectories are simulated using Python's 'solve_ivp' differential equation solver. To start, we manually initialize the robot's position and heading inside the desired geometry in physical space. Then, we locate the motor positions by rotating the heading vector $90°$ and incrementing by δ (half our simulated robot width) in each direction. Once we have the motor locations, we map these points to virtual space and calculate the intensity on each motor by taking the magnitude of the mapping function derivative and it multiplying with the virtual space metric. As intensity is directly proportional to velocity, we can calculate $\frac{dx}{dt}$ and $\frac{dy}{dt}$ by multiplying with the relevant component of the heading vector

$$\frac{dx}{dt} = \cos(\theta)(I_{left} + I_{right})/2 \tag{37}$$

$$\frac{dy}{dt} = \sin(\theta)(I_{left} + I_{right})/2 \tag{38}$$

It is also straightforward to calculate the heading change,

$$\frac{d\theta}{dt} = \frac{(I_{left} - I_{right})}{2\delta} \tag{39}$$

At each timestep, these values are calculated and passed to the solver to initialize the next iteration. Notably, this entire simulation takes place in physical space, only utilizing virtual space to look up the corresponding intensity value.

Microrobot Fabrication. Robots are fabricated massively in parallel using standard semiconductor fabrication tools and techniques as previously demonstrated by our group [23, 64]. To start, we take silicon on insulator (SOI) wafers with a 2 micron (p-type) device layer on top of 500 nm insulating silicon dioxide. These two layers sit on 500 microns of handle silicon. We fabricate photovoltaics by diffusing n-type dopants into the silicon device layer using phosphorus-based spin on glass (Filmtronics P509) in a rapid thermal annealer. We plasma etch mesa structures to expose the underlying p-type silicon, conformally deposit silicon dioxide to insulate the entire sample, and form contacts to the p-type and n-type regions by selectively HF etching the oxide and then sputtering titanium and platinum into the holes. Next, we form interconnects between the photovoltaics and the electrodes that act as the robot's actuator by sputtering titanium and platinum. We encapsulate the entire structure in SU8 for insulation, plasma etch the silicon dioxide layer to define the robot body, and

release robots from the SOI by covering the sample in aluminum and underetching the handle silicon with XeF2 vapor. We then dissolve the aluminum support film to free robots into solution.

Experimental Optical Setup. To form spatially varying intensity fields, we use a commercially available DLP projector (NP-V332W) connected to a computer and display grayscale images corresponding to the control fields. Utilizing the projector's direct mapping between grayscale pixel value (0-255) and the light intensity, projected fields manifest as spatially varying intensity fields on the bottom surface of the petri dish containing our robots. For imaging, we use a DSLR camera (Canon Mark IV EOS) with a macro lens (Laowa 25mm f/2.8 2.5-5X Ultra Macro).

Due to the limitations our optical system and finite turning rate for our robots, we are constrained balancing tasks complexity against image size. We find that in our current projector setup, the smallest optical features we can make are approximately 40x40 um, the size of a single photovoltaic. This constrains the resolution of our intensity profiles, preventing (spatially) small changes in the gradient from contributing effectively to the turning kinematics. For example, near walls and sharp turns, the gradient changes rapidly– an effect which may not be accurately captured in our experimental setup due to the resolution. Further, the robot itself has a finite radius of curvature due to the electrokinetic actuation scheme that prevents sharp, pivot turns even when there is a large difference in intensity on each motor.

Transformation Optics Components as Control Fields. In this work, we utilize a GRIN lens and two spherically-symmetric lenses called the Maxwell fisheye and the Eaton lens. Each of these has a well-defined index of refraction profile utilized in transformation optics. As such, we can directly generate these components as intensity fields for the robot by utilizing the inverse relationship between index of refraction and intensity.

The GRIN lens has a central optical axis with an intensity minimum that spans the length of the lens according to the optical profile

$$n(s) = n_0(1 - \frac{As^2}{2}) \tag{40}$$

where n_0 is the baseline index of refraction value (e.g. 1), A is a constant known as the gradient parameter, and s is the distance from the center optical axis. Light oscillates sinusoidally as it travels through the lens with a consistent period.

The first of the spherically symmetric lenses, the Maxwell fisheye, has an optical profile corresponding to the following equation [49]

$$n(r) = \frac{2}{1 + r^2} \tag{41}$$

where r is the distance from the center point of the lens. Light-like trajectories in these profiles circle the center.

The second spherically symmetric lens is the Eaton lens. It has an approximate profile [65] given by $n(r) \approx (\frac{2}{r} - 1)^{\frac{\theta}{\theta+\pi}}$ where r is the distance to the center of the lens and theta is the desired turning angle.

Extending Results to 3D. While in this work we have focused on robots confined to moving in a plane, many of the underlying concepts can be translated to 3D. As an explicit example, consider a robot that moves with a speed fixed by its position

$$\frac{ds}{dt} = I(x, y, z) \tag{42}$$

along a heading vector $\vec{\chi}$. Treating $\vec{\chi}$ as a three dimensional vector, we seek a generalization of equation 1 that preserves the magnitude of $\vec{\chi}$ under time evolution, depends on the gradient in I, and acts to turn the robot away from regions of high intensity. These conditions can all be satisfied by choosing:

$$\frac{d\vec{\chi}}{dt} = -(\vec{\chi} \times \nabla I) \times \vec{\chi} \tag{43}$$

Heuristically, this equation acts to rotate away from regions where I is large while the cross product ensures the magnitude of $\vec{\chi}$ is clearly fixed. To show it represents a good generalization of equation 1 we can consider what happens when the intensity gradients and heading are purely co-planar. In this case, the term $\vec{\chi} \times \nabla I = \hat{z}(\chi_x \partial_y I - \chi_y \partial_x I) = \hat{z}\chi_i \epsilon_{ij} \partial_j I$ while the second cross product reduces to $-\hat{z} \times \vec{\chi} = \epsilon_{ij}\chi_j$. In other words, when restricted to motion in 2D, we recover eqns. 2 and 1, as anticipated.

To connect this 3D motion to relativistic geodesics in a 3+1 spacetime, we cast the dynamics into a slightly different form by applying the double cross product identity

$$\frac{d}{dt}\vec{\chi}(t) = -\nabla I + \left(\nabla I \cdot \vec{\chi}(t)\right) \vec{\chi}(t). \tag{44}$$

This result makes it clear that the motion of the robot is to descend gradients in the sensory field, subject to the constraint that it preserves the length of the heading. We then compare this result to geodesic equations resulting from treating eqn. 42 as an interval, giving the action principle

$$S = \int d\lambda [(\frac{dt}{d\lambda})^2 I^2(x, y, z) - (\frac{d\vec{x}}{d\lambda})^2] \tag{45}$$

Varying with respect to the spatial coordinates gives

$$\frac{d}{d\lambda}[-\frac{dx_i}{d\lambda}] = I\partial_i I(\frac{dt}{d\lambda})^2 \tag{46}$$

Again, using the affine parametrization [34] $d\lambda = I^2 dt$ we find

$$\frac{d}{dt}[-\frac{dx_i}{dt}\frac{1}{I^2}] = \frac{\partial_i I}{I} \tag{47}$$

We now note that $\frac{dx}{dt}/I = \chi_x$, letting us factor terms on the LHS to yield

$$\frac{d}{dt}[-\chi_x \frac{1}{I}] = \frac{\partial_i I}{I} \tag{48}$$

18

After applying the chain rule and re-arranging we find

$$\frac{d\chi_x}{dt} = -\partial_i I + \chi_x(\partial_l I \chi_l) \qquad (49)$$

The same derivation applies for all spatial components. When we merge these results by explicitly writing them in vector form, we reproduce the robot's governing equation for its heading vector (i.e. eqn 44):

$$\frac{d\vec{\chi}}{dt} = -\nabla I + \vec{\chi}(\nabla I \cdot \vec{\chi}) \qquad (50)$$

Thus, the simple dynamics of a robot following equations 44 and 42 both generalize the 2D motion studied here and are formally identical to light rays in a fully 3+1 dimensional spacetime.

Declarations

- Funding: Army Research Office (ARO YIP W911NF-17-S-0002), the Sloan Foundation, the Packard Foundation
- Competing interests: The authors declare no competing interests.
- Ethics approval and consent to participate: Not applicable
- Consent for publication: The authors consent to publish under the CC-BY Open Access License.
- Data availability: Experimental data is provided as supplemental videos, but raw image files are available upon request.
- Materials availability: Not applicable
- Code availability: Code to simulate robot trajectories will be hosted on Github (https://github.com/whreinhardt/).
- Author contribution: W.H.R and M.Z.M designed the research. W.H.R fabricated the robots, wrote the simulation, performed experiments, and analyzed data. M.Z.M conceived of the original idea, developed the theory, and supervised research. W.H.R and M.Z.M wrote the paper.

References

[1] Bradley J Nelson, Ioannis K Kaliakatsos, and Jake J Abbott. Microrobots for minimally invasive medicine. *Annual review of biomedical engineering*, 12(1): 55–85, 2010. Publisher: Annual Reviews.

[2] Veronica Iacovacci, Eric Diller, Daniel Ahmed, and Arianna Menciassi. Medical microrobots. *Annual Review of Biomedical Engineering*, 26, 2024. Publisher: Annual Reviews.

[3] Mohammad Zarei and Mohanna Zarei. Self-propelled micro/nanomotors for sensing and environmental remediation. *Small*, 14(30):1800912, 2018. Publisher: Wiley Online Library.

[4] Mario Urso, Martina Ussia, and Martin Pumera. Smart micro-and nanorobots for water purification. *Nature Reviews Bioengineering*, 1(4):236–251, 2023. Publisher: Nature Publishing Group UK London.

[5] Zhuoran Zhang, Xian Wang, Jun Liu, Changsheng Dai, and Yu Sun. Robotic micromanipulation: Fundamentals and applications. *Annual Review of Control, Robotics, and Autonomous Systems*, 2(1):181–203, 2019. Publisher: Annual Reviews.

[6] Dandan Zhang, Antoine Barbot, Benny Lo, and Guang-Zhong Yang. Distributed Force Control for Microrobot Manipulation via Planar Multi-Spot Optical Tweezer. *Advanced Optical Materials*, 8(21): 2000543, 2020. ISSN 2195-1071. doi: 10.1002/adom.202000543. URL https://onlinelibrary.wiley.com/doi/abs/10.1002/adom.202000543. _eprint: https://onlinelibrary.wiley.com/doi/pdf/10.1002/adom.202000543.

[7] Eric Diller, Joshua Giltinan, and Metin Sitti. Independent control of multiple magnetic microrobots in three dimensions. *The International Journal of Robotics Research*, 32(5):614–631, April 2013. ISSN 0278-3649. doi: 10.1177/0278364913483183. URL https://doi.org/10.1177/0278364913483183. Publisher: SAGE Publications Ltd STM.

[8] Ambarish Ghosh and Peer Fischer. Controlled Propulsion of Artificial Magnetic Nanostructured Propellers. *Nano Letters*, 9(6):2243–2245, June 2009. ISSN 1530-6984. doi: 10.1021/nl900186w. URL https://doi.org/10.1021/nl900186w. Publisher: American Chemical Society.

[9] Dominic R. Frutiger, Karl Vollmers, Bradley E. Kratochvil, and Bradley J. Nelson. Small, Fast, and Under Control: Wireless Resonant Magnetic Microagents. *The International Journal of Robotics Research*, 29(5):613–636, April 2010. ISSN 0278-3649. doi: 10.1177/0278364909353351. URL https://doi.org/10.1177/0278364909353351. Publisher: SAGE Publications Ltd STM.

[10] Islam S. M. Khalil, Marc P. Pichel, Leon Abelmann, and Sarthak Misra. Closed-loop control of magnetotactic bacteria. *The International Journal of Robotics Research*, 32(6):637–649, May 2013. ISSN 0278-3649. doi: 10.1177/0278364913479412. URL https://doi.org/10.1177/0278364913479412. Publisher: SAGE Publications Ltd STM.

[11] Daniel Ahmed, Mengqian Lu, Amir Nourhani, Paul E. Lammert, Zak Stratton, Hari S. Muddana, Vincent H. Crespi, and Tony Jun Huang. Selectively manipulable acoustic-powered microswimmers. *Scientific Reports*, 5(1):9744, May 2015. ISSN 2045-2322. doi: 10.1038/srep09744. URL https://www.nature.com/articles/srep09744.

[12] Daniel Ahmed, Cornel Dillinger, Ayoung Hong, and Bradley J. Nelson. Artificial Acousto-Magnetic Soft Microswimmers. *Advanced Materials Technologies*, 2(7):1700050, 2017. ISSN 2365-709X. doi: 10.1002/admt.201700050. URL https://onlinelibrary.wiley.com/doi/abs/10.1002/admt.201700050. _eprint: https://onlinelibrary.wiley.com/doi/pdf/10.1002/admt.201700050.

[13] Alexia Del Campo Fonseca, Chaim Glück, Jeanne Droux, Yann Ferry, Carole Frei, Susanne Wegener, Bruno Weber, Mohamad El Amki, and Daniel Ahmed. Ultrasound trapping and navigation of microrobots in the mouse brain vasculature. *Nature Communications*, 14(1):5889, September 2023. ISSN 2041-1723. doi: 10.1038/s41467-023-41557-3. URL https://www.nature.com/articles/s41467-023-41557-3. Publisher: Nature Publishing Group.

[14] Jialin Jiang, Zhengxin Yang, Antoine Ferreira, and Li Zhang. Control and Autonomy of Microrobots: Recent Progress and Perspective. *Advanced Intelligent Systems*, 4(5):2100279, 2022. ISSN 2640-4567. doi: 10.1002/aisy.202100279. URL https://onlinelibrary.wiley.com/doi/abs/10.1002/aisy.202100279. _eprint: https://onlinelibrary.wiley.com/doi/pdf/10.1002/aisy.202100279.

[15] Sagar Chowdhury, Wuming Jing, and David J. Cappelleri. Controlling multiple microrobots: recent progress and future challenges. *Journal of Micro-Bio Robotics*, 10(1):1–11, October 2015. ISSN 2194-6426. doi: 10.1007/s12213-015-0083-6. URL https://doi.org/10.1007/s12213-015-0083-6.

[16] Ming You, Chuanrui Chen, Leilei Xu, Fangzhi Mou, and Jianguo Guan. Intelligent Micro/nanomotors with Taxis. *Accounts of Chemical Research*, 51(12):3006–3014, December 2018. ISSN 0001-4842. doi: 10.1021/acs.accounts.8b00291. URL https://doi.org/10.1021/acs.accounts.8b00291. Publisher: American Chemical Society.

[17] Hoyeon Kim and Min Jun Kim. Electric Field Control of Bacteria-Powered Microrobots Using a Static Obstacle Avoidance Algorithm. *IEEE Transactions on Robotics*, 32(1):125–137, February 2016. ISSN 1941-0468. doi: 10.1109/TRO.2015.2504370. URL https://ieeexplore.ieee.org/document/7365478/?arnumber=7365478. Conference Name: IEEE Transactions on Robotics.

[18] Steven Ceron, Gaurav Gardi, Kirstin Petersen, and Metin Sitti. Programmable self-organization of heterogeneous microrobot collectives. *Proceedings of the National Academy of Sciences*, 120(24):e2221913120, June 2023. doi: 10.1073/pnas.2221913120. URL https://www.pnas.org/doi/full/10.1073/pnas.2221913120. Publisher: Proceedings of the National Academy of Sciences.

[19] Fengtong Ji, Yilin Wu, Martin Pumera, and Li Zhang. Collective behaviors of active matter learning from natural taxes across scales. *Advanced Materials*, 35 (8):2203959, 2023. Publisher: Wiley Online Library.

[20] Gaurav Gardi, Steven Ceron, Wendong Wang, Kirstin Petersen, and Metin Sitti. Microrobot collectives with reconfigurable morphologies, behaviors, and functions. *Nature communications*, 13(1):2239, 2022. Publisher: Nature Publishing Group UK London.

[21] Hong Wang and Martin Pumera. Coordinated behaviors of artificial micro-/nanomachines: from mutual interactions to interactions with the environment. *Chemical Society Reviews*, 49(10):3211–3230, 2020. Publisher: Royal Society of Chemistry.

[22] Roberto Di Leonardo, Nicola Pellicciotta, Ojus S. Bagal, Viridiana Carmona Sosa, Giacomo Frangipane, and Gaszton Vizsnyiczai. Biohybrid microbots driven by light. In *Optical Trapping and Optical Micromanipulation XX*, volume PC12649, page PC126490B. SPIE, October 2023. doi: 10.1117/12.2682753. URL https://www.spiedigitallibrary.org/conference-proceedings-of-spie/PC12649/

PC126490B/Biohybrid-microbots-driven-by-light/10.1117/12.2682753.full.

[23] Lucas C. Hanson, William H. Reinhardt, Scott Shrager, Tarunyaa Sivakumar, and Marc Z. Miskin. Electrokinetic Propulsion for Electronically Integrated Microscopic Robots, September 2024. URL http://arxiv.org/abs/2409.07293. arXiv:2409.07293 [cs].

[24] Jiang Zhuang, Rika Wright Carlsen, and Metin Sitti. pH-Taxis of Biohybrid Microsystems. *Scientific Reports*, 5(1):11403, June 2015. ISSN 2045-2322. doi: 10.1038/srep11403. URL https://www.nature.com/articles/srep11403. Publisher: Nature Publishing Group.

[25] Chao Gao, Ye Feng, Daniela A. Wilson, Yingfeng Tu, and Fei Peng. Micro-Nano Motors with Taxis Behavior: Principles, Designs, and Biomedical Applications. *Small*, 18(15):2106263, 2022. ISSN 1613-6829. doi: 10.1002/smll.202106263. URL https://onlinelibrary.wiley.com/doi/abs/10.1002/smll.202106263. _eprint: https://onlinelibrary.wiley.com/doi/pdf/10.1002/smll.202106263.

[26] Anis Naema Atiyah Rafai, Noraziah Adzhar, and Nor Izzati Jaini. A Review on Path Planning and Obstacle Avoidance Algorithms for Autonomous Mobile Robots. *Journal of Robotics*, 2022(1): 2538220, 2022. ISSN 1687-9619. doi: 10.1155/2022/2538220. URL https://onlinelibrary.wiley.com/doi/abs/10.1155/2022/2538220. _eprint: https://onlinelibrary.wiley.com/doi/pdf/10.1155/2022/2538220.

[27] Aziz ur Rehman, Ahsan Tanveer, M. Touseef Ashraf, and Umer Khan. Motion Planning for Autonomous Ground Vehicles Using Artificial Potential Fields: A Review, October 2023. URL http://arxiv.org/abs/2310.14339. arXiv:2310.14339 [cs].

[28] Jean-François Duhé, Stéphane Victor, and Pierre Melchior. ContribUtions on Artificial Potential Field Method for Effective Obstacle Avoidance. *Fractional Calculus and Applied Analysis*, 24(2):421–446, April 2021. ISSN 1314-2224. doi: 10.1515/fca-2021-0019. URL https://doi.org/10.1515/fca-2021-0019.

[29] Scott Hotton and Jeff Yoshimi. *The Open Dynamics of Braitenberg Vehicles*. MIT Press, June 2024. ISBN 978-0-262-54819-9. Google-Books-ID: jbTXEAAAQBAJ.

[30] Sean Carroll. *Spacetime and geometry: an introduction to general relativity*. Addison Wesley, San Francisco, 2004. ISBN 978-0-8053-8732-2.

[31] Ulf Leonhardt and Thomas G. Philbin. Transformation Optics and the Geometry of Light, June 2008. URL http://arxiv.org/abs/0805.4778. arXiv:0805.4778 [physics].

[32] Shengkai Li, Hussain N Gynai, Steven W Tarr, Emily Alicea-Muñoz, Pablo Laguna, Gongjie Li, and Daniel I Goldman. A robophysical model of spacetime dynamics. *Scientific Reports*, 13(1):21589, 2023. Publisher: Nature Publishing Group UK London.

[33] Shengkai Li, Yasemin Ozkan-Aydin, Charles Xiao, Gabriella Small, Hussain N. Gynai, Gongjie Li, Jennifer M. Rieser, Pablo Laguna, and Daniel I. Goldman. Field-mediated locomotor dynamics on highly deformable surfaces. *Proceedings of the National Academy of Sciences*, 119(30):e2113912119, July 2022. ISSN 0027-8424, 1091-6490. doi: 10.1073/pnas.2113912119. URL https://pnas.org/doi/full/10.1073/pnas.2113912119.

[34] Matt Visser. Efficient computation of null affine parameters, December 2023. URL http://arxiv.org/abs/2211.07835. arXiv:2211.07835 [gr-qc].

[35] E. J. Post. *Formal Structure of Electromagnetics: General Covariance and Electromagnetics*. Courier Corporation, January 1997. ISBN 978-0-486-65427-0. Google-Books-ID: zXeuy8psmegC.

[36] Ulf Leonhardt. Optical Conformal Mapping. *Science*, 312(5781):1777–1780, June 2006. doi: 10.1126/science.1126493. URL https://www.science.org/doi/10.1126/science.1126493. Publisher: American Association for the Advancement of Science.

[37] Lin Xu and Huanyang Chen. Conformal transformation optics. *Nature Photonics*, 9(1):15–23, January 2015. ISSN 1749-4893. doi: 10.1038/nphoton.2014.307. URL https://www.nature.com/articles/nphoton.2014.307. Publisher: Nature Publishing Group.

[38] Jeremiah P. Turpin, Ayah T. Massoud, Zhi Hao Jiang, Pingjuan L. Werner, and Douglas H. Werner. Conformal mappings to achieve simple material parameters for transformation optics devices. *Optics Express*, 18(1):244–252, January 2010. ISSN 1094-4087. doi: 10.1364/OE.18.000244. URL https://opg.optica.org/oe/abstract.cfm?uri=oe-18-1-244. Publisher: Optica Publishing Group.

[39] Lloyd N. Trefethen. Numerical Conformal Mapping with Rational Functions. *Computational Methods and Function Theory*, 20(3):369–387, November 2020. ISSN 2195-3724. doi: 10.1007/s40315-020-00325-w. URL https://doi.org/10.1007/s40315-020-00325-w.

[40] Tobin A. Driscoll and Lloyd N. Trefethen. *Schwarz-Christoffel Mapping*. Cambridge Monographs on Applied and Computational Mathematics. Cambridge University Press, Cambridge, 2002. ISBN 978-0-521-80726-5. doi: 10.1017/CBO9780511546808. URL https://www.cambridge.org/core/books/schwarzchristoffel-mapping/E8439E14F3CFE0F8CC2943217A5CA4C4.

[41] Tobin A. Driscoll. Algorithm 756: a MATLAB toolbox for Schwarz-Christoffel mapping. *ACM Trans. Math. Softw.*, 22(2):168–186, June 1996. ISSN 0098-3500. doi: 10.1145/229473.229475. URL https://dl.acm.org/doi/10.1145/229473.229475.

[42] Shuai Xiong, Yijun Feng, Tian Jiang, and Junming Zhao. Designing retrodirective reflector on a planar surface by transformation optics. *AIP Advances*, 3(1):012113, January 2013. ISSN 2158-3226. doi: 10.1063/1.4789406. URL https://doi.org/10.1063/1.4789406.

[43] I. Gallina, G. Castaldi, and V. Galdi. Transformation Media for Thin Planar Retrodirective Reflectors. *IEEE Antennas and Wireless Propagation Letters*, 7:603–605, 2008. ISSN 1536-1225. doi: 10.1109/LAWP.2008.2003541. URL https://ieeexplore.ieee.org/document/4595645. Place: New York Publisher: IEEE.

[44] Fateme Nazarzadeh and Abbas Ali Heidari. Wideband flat reflector antenna based on conformal transformation optics. *Optik*, 264:169429, August 2022. ISSN 0030-4026. doi: 10.1016/j.ijleo.2022.169429. URL https://www.sciencedirect.com/science/article/pii/S003040262200746X.

[45] Liang Liang and Sean V. Hum. Wide-angle scannable reflector design using conformal transformation optics. *Optics Express*, 21(2):2133–2146, January 2013.

ISSN 1094-4087. doi: 10.1364/OE.21.002133. URL https://opg.optica.org/oe/abstract.cfm?uri=oe-21-2-2133. Publisher: Optica Publishing Group.

[46] Kyu-Tae Lee, Chengang Ji, Hideo Iizuka, and Debasish Banerjee. Optical cloaking and invisibility: From fiction toward a technological reality. *Journal of Applied Physics*, 129(23):231101, June 2021. ISSN 0021-8979. doi: 10.1063/5.0048846. URL https://doi.org/10.1063/5.0048846.

[47] Fei Sun, Bin Zheng, Hongsheng Chen, Wei Jiang, Shuwei Guo, Yichao Liu, Yungui Ma, and Sailing He. Transformation Optics: From Classic Theory and Applications to its New Branches. *Laser & Photonics Reviews*, 11(6):1700034, 2017. ISSN 1863-8899. doi: 10.1002/lpor.201700034. URL https://onlinelibrary.wiley.com/doi/abs/10.1002/lpor.201700034. _eprint: https://onlinelibrary.wiley.com/doi/pdf/10.1002/lpor.201700034.

[48] Pekka Alitalo and Sergei Tretyakov. Electromagnetic cloaking with metamaterials. *Materials Today*, 12(3):22–29, March 2009. ISSN 1369-7021. doi: 10.1016/S1369-7021(09)70072-0. URL https://www.sciencedirect.com/science/article/pii/S1369702109700720.

[49] Tomáš Tyc, Lenka Herzánová, Martin Šarbort, and Klaus Bering. Absolute instruments and perfect imaging in geometrical optics. *New Journal of Physics*, 13(11):115004, November 2011. ISSN 1367-2630. doi: 10.1088/1367-2630/13/11/115004. URL https://iopscience.iop.org/article/10.1088/1367-2630/13/11/115004.

[50] C. Gomez-Reino, M.v. Perez, C. Bao, and M.t. Flores-Arias. Design of GRIN optical components for coupling and interconnects. *Laser & Photonics Reviews*, 2(3):203–215, 2008. ISSN 1863-8899. doi: 10.1002/lpor.200810002. URL https://onlinelibrary.wiley.com/doi/abs/10.1002/lpor.200810002. _eprint: https://onlinelibrary.wiley.com/doi/pdf/10.1002/lpor.200810002.

[51] Sébastien Bouchard and Simon Thibault. GRIN planar waveguide concentrator used with a single axis tracker. *Optics Express*, 22(102):A248–A258, March 2014. ISSN 1094-4087. doi: 10.1364/OE.22.00A248. URL https://opg.optica.org/oe/abstract.cfm?uri=oe-22-S2-A248. Publisher: Optica Publishing Group.

[52] Eugene Hecht. *Optics*. Pearson Education, Inc, Boston, 5 ed edition, 2017. ISBN 978-0-13-397722-6.

[53] Cun-Hua Zhao. Analytic Solution for an Eaton Lens for Rotating 90°. *Current Optics and Photonics*, 4(4):326–329, August 2020. doi: 10.3807/COPP.2020.4.4.326. URL https://doi.org/10.3807/COPP.2020.4.4.326.

[54] Jen Yung Li. The 90° Rotating Eaton Lens Synthesized by Metasurfaces. URL https://ieeexplore.ieee.org/document/8367795.

[55] Li Xu, Maya Lassiter, Xiao Wu, Yejoong Kim, Jungho Lee, Makoto Yasuda, Masaru Kawaminami, Marc Miskin, David Blaauw, and Dennis Sylvester. A 210x340x50 um Integrated CMOS System for Micro-Robots with Energy Harvesting, Sensing, Processing, Communication and Actuation. In *2022 IEEE International Solid-State Circuits Conference (ISSCC)*, volume 65, pages 1–3, February 2022. doi: 10.1109/ISSCC42614.2022.9731743. URL https://ieeexplore.ieee.org/abstract/document/9731743/references#references. ISSN: 2376-8606.

24

[56] Michael F. Reynolds, Alejandro J. Cortese, Qingkun Liu, Zhangqi Zheng, Wei Wang, Samantha L. Norris, Sunwoo Lee, Marc Z. Miskin, Alyosha C. Molnar, Itai Cohen, and Paul L. McEuen. Microscopic robots with onboard digital control. *Science Robotics*, 7(70):eabq2296, September 2022. doi: 10.1126/scirobotics. abq2296. URL https://www.science.org/doi/10.1126/scirobotics.abq2296. Publisher: American Association for the Advancement of Science.

[57] Nader Engheta. Four-dimensional optics using time-varying metamaterials. *Science*, 379(6638):1190–1191, March 2023. doi: 10.1126/science.adf1094. URL https://www.science.org/doi/full/10.1126/science.adf1094. Publisher: American Association for the Advancement of Science.

[58] Ulf Leonhardt and Thomas G Philbin. Transformation optics and the geometry of light. In *Progress in optics*, volume 53, pages 69–152. Elsevier, 2009.

[59] Carlos Barcelo, Stefano Liberati, and Matt Visser. Analogue gravity. *Living reviews in relativity*, 14:1–159, 2011. Publisher: Springer.

[60] Ying Feng, Miao An, Yang Liu, Muhammad Tariq Sarwar, and Huaming Yang. Advances in Chemically Powered Micro/Nanorobots for Biological Applications: A Review. *Advanced Functional Materials*, 33 (1):2209883, 2023. ISSN 1616-3028. doi: 10.1002/adfm.202209883. URL https://onlinelibrary.wiley.com/doi/abs/10.1002/adfm.202209883. _eprint: https://onlinelibrary.wiley.com/doi/pdf/10.1002/adfm.202209883.

[61] Yuxing Ji, Xiankun Lin, Hongyue Zhang, Yingjie Wu, Junbai Li, and Qiang He. Thermoresponsive Polymer Brush Modulation on the Direction of Motion of Phoretically Driven Janus Micromotors. *Angewandte Chemie*, 131(13):4228–4232, 2019. ISSN 1521-3757. doi: 10.1002/ange.201812860. URL https://onlinelibrary.wiley.com/doi/abs/10.1002/ange.201812860. _eprint: https://onlinelibrary.wiley.com/doi/pdf/10.1002/ange.201812860.

[62] Jack A Defay, Alexandra Q Nilles, and Kirstin Petersen. Characterization of the design space of collective Braitenberg vehicles. In *International Symposium on Distributed Autonomous Robotic Systems*, pages 257–272. Springer, 2022.

[63] Melvin Gauci, Jianing Chen, Wei Li, Tony J Dodd, and Roderich Groß. Self-organized aggregation without computation. *The International Journal of Robotics Research*, 33(8):1145–1161, 2014. Publisher: SAGE Publications Sage UK: London, England.

[64] Marc Z. Miskin, Alejandro J. Cortese, Kyle Dorsey, Edward P. Esposito, Michael F. Reynolds, Qingkun Liu, Michael Cao, David A. Muller, Paul L. McEuen, and Itai Cohen. Electronically integrated, mass-manufactured, microscopic robots. *Nature*, 584(7822):557–561, August 2020. ISSN 1476-4687. doi: 10.1038/s41586-020-2626-9. URL https://www.nature.com/articles/s41586-020-2626-9. Number: 7822 Publisher: Nature Publishing Group.

[65] Sang-Hoon Kim. Retroreflector Approximation of a Generalized Eaton Lens. *Journal of Modern Optics*, 59(9):839–842, May 2012. ISSN 0950-0340, 1362-3044. doi: 10.1080/09500340.2012.675089. URL http://arxiv.org/abs/1112.2754. arXiv:1112.2754 [physics].